

Dual-Phase Single-Ion Pathway Interfaces for Robust Lithium Metal in Working Batteries

Rui Xu, Ye Xiao, Rui Zhang, Xin-Bing Cheng, Chen-Zi Zhao, Xue-Qiang Zhang, Chong Yan, Qiang Zhang, and Jia-Qi Huang*

The lithium (Li) metal anode is confronted by severe interfacial issues that strongly hinder its practical deployment. The unstable interfaces directly induce unfavorable low cycling efficiency, dendritic Li deposition, and even strong safety concerns. An advanced artificial protective layer with single-ion pathways holds great promise for enabling a spatially homogeneous ionic and electric field distribution over Li metal surface, therefore well protecting the Li metal anode during long-term working conditions. Herein, a robust dual-phase artificial interface is constructed, where not only the single-ion-conducting nature, but also high mechanical rigidity and considerable deformability can be fulfilled simultaneously by the rational integration of a garnet Al-doped $\text{Li}_{6.75}\text{La}_3\text{Zr}_{1.75}\text{Ta}_{0.25}\text{O}_{12}$ -based bottom layer and a lithiated Nafion top layer. The as-constructed artificial solid electrolyte interphase is demonstrated to significantly stabilize the repeated cell charging/discharging process via regulating a facile Li-ion transport and a compact Li plating behavior, hence contributing to a higher coulombic efficiency and a considerably enhanced cyclability of lithium metal batteries. This work highlights the significance of rational manipulation of the interfacial properties of a working Li metal anode and affords fresh insights into achieving dendrite-free Li deposition behavior in a working battery.

With the ever-emerging high expectation on energy density from the cutting-edge consumer electronics, electric vehicles, and smart grids, exploring advanced energy storage systems with exceptional high energy density has been strongly considered.^[1] Nevertheless, the state-of-the-art lithium-ion batteries

(LIBs), approaching a ceiling energy density of 300 Wh kg^{-1} , can no longer catch up with the surgent pursuing trend.^[2] Based on a plating/stripping mechanism instead of intercalation chemistry, Li metal anodes possess an extremely high theoretical specific capacity (3860 mAh g^{-1}) and the lowest equilibrium potential (-3.040 V vs standard hydrogen electrode) among various anodes, which holds the promise to be paired with sulfur (S) and oxygen (O_2) cathodes to deliver a three to five times increase in energy density relative to the conventional LIBs.^[3]

Attempts to apply Li metal anodes date back to the 1970s. The low cycling efficiency and poor safety issue originating from dendritic Li deposition have placed a huge concern in rechargeable lithium metal batteries (LMBs) since then.^[4] To get rid of the intrinsic drawbacks of Li metal anodes and fully suppress the dendrite formation, tremendous investigations have been conducted to probe the Li/electrolyte interphases, the properties

of which are reported to directly determine Li nucleation and growing patterns.^[5]

Generally, the components in nonaqueous liquid electrolyte incline to be reduced by the highly reactive Li metal, resulting in the spontaneous formation of a solid electrolyte interphase (SEI) between the lithium metal and the electrolyte.^[6] Nevertheless, the as-formed native SEI is chemically heterogeneous and structurally unstable, which inevitably gives rise to a nonuniform interfacial Li^+ flux and consequently causes the undesirable filament-like Li dendrite growth.^[7] Inorganics-rich SEI has been regarded as a more desirable choice to enhance the interfacial stability of Li metal anode considering its high mechanical strength and rapid lithium-ion diffusion pathways.^[8] Unfortunately, the brittle inorganics-rich SEI is prone to be ruptured when a huge volume variation is occurred during the repeated plating/stripping of Li metal, which claims the failure of Li metal protection during a long-term cycling.^[9] The broken sites with shorter ion transfer pathways become “hot spots” to favor local ion enrichment, thereafter promoting dendrite nucleation and growth.^[10] In this consideration, extensive structured hosts have been proposed to alleviate the enormous volume expansion during repeated Li plating/stripping processes to guarantee stable interface,

R. Xu, Y. Xiao, C. Yan, Prof. J.-Q. Huang
School of Materials Science and Engineering
Beijing Institute of Technology
Beijing 100081, China
E-mail: jqhuang@bit.edu.cn

R. Xu, Y. Xiao, C. Yan, Prof. J.-Q. Huang
Advanced Research Institute of Multidisciplinary Science
Beijing Institute of Technology
Beijing 100081, China

R. Zhang, Dr. X.-B. Cheng, C.-Z. Zhao, X.-Q. Zhang, Prof. Q. Zhang
Beijing Key Laboratory of Green Chemical Reaction Engineering and Technology
Department of Chemical Engineering
Tsinghua University
Beijing 100084, China

 The ORCID identification number(s) for the author(s) of this article can be found under <https://doi.org/10.1002/adma.201808392>.

DOI: 10.1002/adma.201808392

which is widely accepted as an effective strategy for developing safe and high-energy-density lithium batteries.^[11] For example, sparked reduced graphene oxide was investigated as a Li metal host by Cui and co-workers, which not only provides a stable scaffold for Li plating/stripping, but also contributes to excellent lithiophilicity for uniform Li infusion and deposition.^[11f] Actually, if a robust artificial protective interface is enabled with high uniformity, sufficient rigidity, and considerable deformability concurrently, a stabilized Li metal anode can be hopefully expected in the working rechargeable LMBs.^[12]

Besides the heterogeneous nature of the SEI, which induces uneven Li-ion transfer, the effects of space charge regions generated by ion depletion on the dendrite proliferation have been highly valued.^[13] The dissolved Li salts release mobile Li^+ and anions in routine nonaqueous electrolytes. However, the field-induced transfer of electrochemical active Li^+ with larger solvation cluster is much slower than that of the counterions, which reflects as a low Li-ion transference number (t_{Li^+} , 0.2–0.4) in most liquid electrolytes.^[14] The low t_{Li^+} will impose a large Li-ion concentration gradient at the vicinity of Li anode, hence leading to the buildup of a strong interfacial electric field and an exacerbated dendrite propagation (Figure 1a). This becomes even more severe under rather high current densities.^[15] To this end, emerging electrolytes with high Li-ion transference number are highly pursued and extensively explored during the past decades.^[16]

In this contribution, we propose a dual-phase single-ion-conducting artificial interface to protect the Li metal anode in a working battery. A robust inorganics-rich artificial interface can be achieved by rational integration of rigid garnet Al-doped $\text{Li}_{6.75}\text{La}_3\text{Zr}_{1.75}\text{Ta}_{0.25}\text{O}_{12}$ (LLZTO) and soft lithiated Nafion (Li-Nafion) components. Both garnet-type LLZTO and Li-Nafion were chosen in this work due to their single-ion-conductive nature

and high chemical/electrochemical compatibility against Li metal.^[17] In details, the garnet Al-doped LLZTO-based bottom layer maintains the high mechanical rigidity and rapid Li^+ transport ability of the protective film,^[18] while the Li-Nafion top layer endows the film with considerable elasticity to deform with the volume fluctuation of the electrode. The unique dual-layer LLZTO/Li-Nafion (denoted as LLN) artificial film with nearly unity t_{Li^+} is expected to modulate a homogeneous and high-efficiency Li^+ diffusion manner at the surface of Li anode, subsequently in favor of a compact and dense Li plating pattern (Figure 1b).

The dual-layered LLN coating herein was fabricated via a facile doctor blading method. X-ray diffraction characterization was conducted on the as-prepared LLZTO bottom layer, where a well-maintained cubic phase can be observed (Figure S1, Supporting Information). Note that a small portion (10 wt%) of Li-Nafion as a binder was incorporated in the bottom layer to effectively connect the LLZTO particles and diminish the contact resistance between LLZTO and Li metal.^[19] The particle size of LLZTO was determined to be about 66 nm (Figure S2, Supporting Information). The lithiation of Nafion was performed to reduce the Li^+ transfer barrier while enhancing its stability against Li metal, which can be confirmed by the arising peak at around 1630 cm^{-1} in the Fourier transform infrared spectroscopy spectrum, indicating the successful substitution of H^+ by Li^+ (Figure S3, Supporting Information).^[20]

The protective layer with dual-layer architecture is composed of a $4\text{ }\mu\text{m}$ thick ceramic bottom layer and a $1\text{ }\mu\text{m}$ thick Li-Nafion top layer according to the cross-sectional scanning electron microscopy (SEM) observation (Figure 2a). The top Li-Nafion layer with high uniformity well covered the compact bottom layer from the top-view images and the corresponding element mappings as displayed in Figure S4 (Supporting Information), which equips the LLN film with considerable deformability

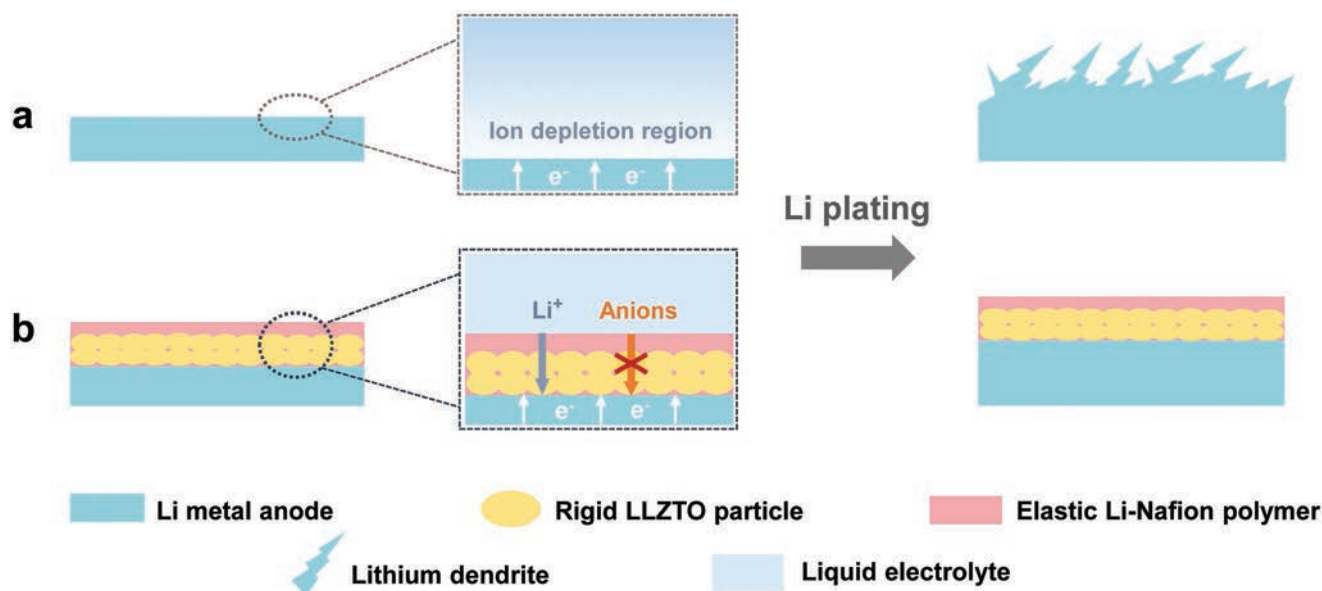


Figure 1. Schematic illustrations of different Li deposition patterns. a) The space charge region induced by anion depletion will impose a strong electric field at the vicinity of bare Li, leading to dendritic Li deposits. b) After incorporating the single-ion-conducting LLN coating composed of rigid LLZTO and elastic Li-Nafion, a uniform and compact Li plating behavior can be obtained.

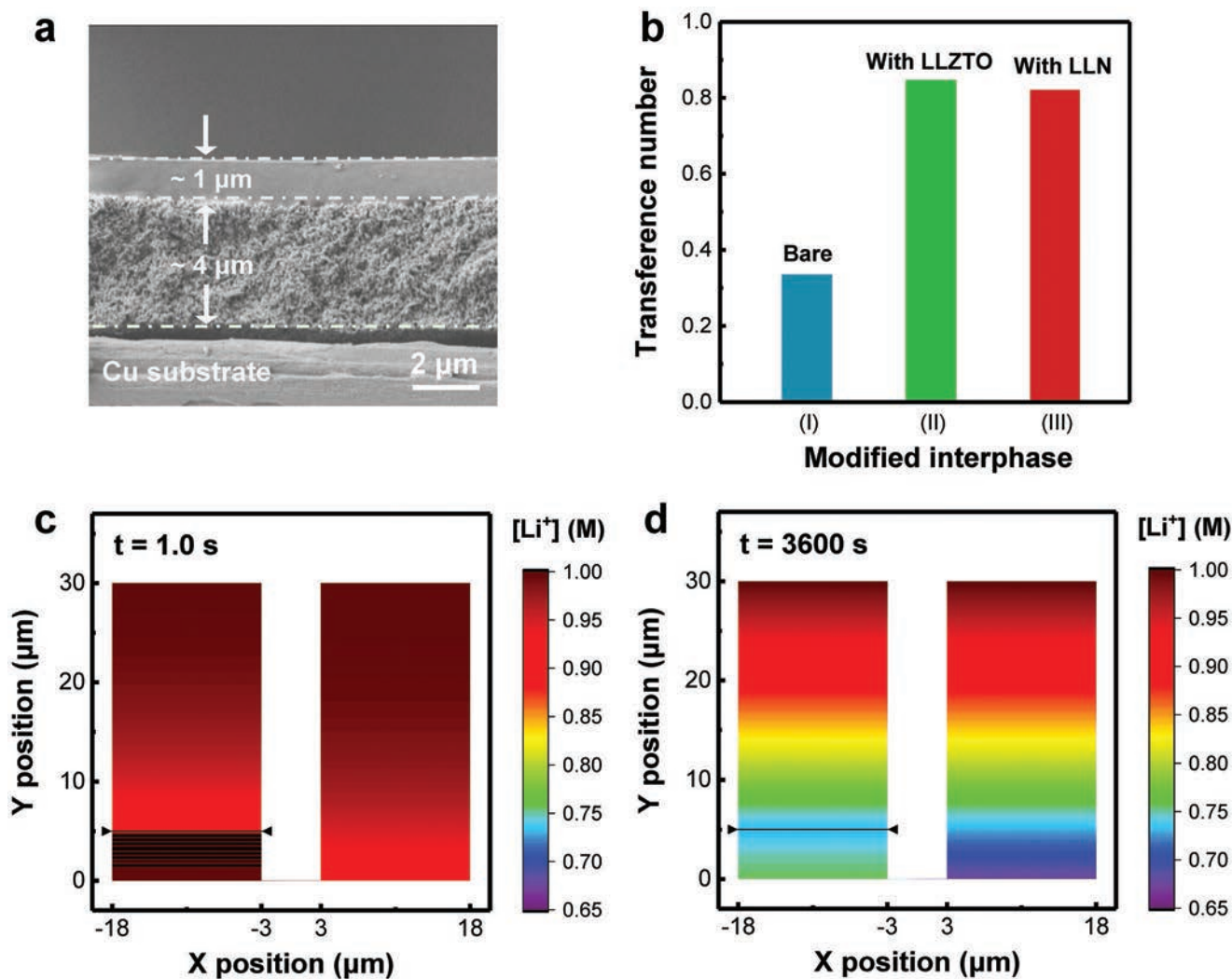


Figure 2. Morphological and ion-transport characterizations of the LLN film. a) Side-view SEM image of the dual-layered LLN with Li-Nafion top layer and LLZTO-based bottom layer. b) A comparison of Li-ion transference number with various modification routes on Li electrodes. c,d) FEM simulation results of Li-ion concentration distribution from bulk electrolyte to anode surface at the initial state (1.0 s) (c) and at a prolonged steady state (3600 s) (d) during the galvanostatic process with (left)/without (right) a 5 μm -thick single-ion-conductive protective film.

to avoid mechanical breakdown during repeated charging/discharging processes.

The ionic conductivity of the LLN protective layer was measured at room temperature using blocking electrode method. A considerable value of $3.0 \times 10^{-5} \text{ S cm}^{-1}$ can be determined (Figure S5, Supporting Information), which is slightly lower than individual cubic-phase LLZTO with an ionic conductivity of $\approx 10^{-4} \text{ S cm}^{-1}$ as reported.^[21] The t_{Li^+} measurement was further conducted to quantitatively describe the single-ion-conducting ability of the LLN coating layer. In the case of bare symmetric Li cell with conventional carbonate electrolyte (1.0 M $\text{LiPF}_6\text{-EC/DEC}$, $v/v = 1:1$), a rather low t_{Li^+} of 0.33 was obtained (Figure S6a, Supporting Information) owing to the faster migration speed of anions than solvated Li^+ , which is consistent with previous reports.^[22] However, t_{Li^+} can be dramatically improved to 0.82 after the incorporation of LLN coating layer (Figure S6b, Supporting Information). A comprehensive comparison of t_{Li^+} with/without modifications and the related data for the t_{Li^+}

determination are listed in Figure 2b and Table S1 (Supporting Information), respectively.

Finite element method (FEM) simulations were carried out to provide insightful understandings on spatial Li-ion concentration distributions when single-ion pathways are present at Li anode surface (Figure 2c,d, and Figure S7 and Movie S1, Supporting Information). In common nonaqueous electrolytes with a low t_{Li^+} , the reverse migration of anions under applied electric field will evidently interfere cation diffusion. As a result, a large Li^+ concentration gradient is generated from bulk electrolyte to anode vicinity after a prolonged galvanostatic process. However, this phenomenon can be considerably alleviated after incorporating a single-ion-conductive protective film. Li ions tend to be attracted to the interface where the immobilization of anion contributes to a more efficient Li^+ transfer mode, replenishing the electrode/electrolyte interface with abundant and homogeneous Li-ion flux.^[23] The suppressed ion concentration gradient and uniformized ion

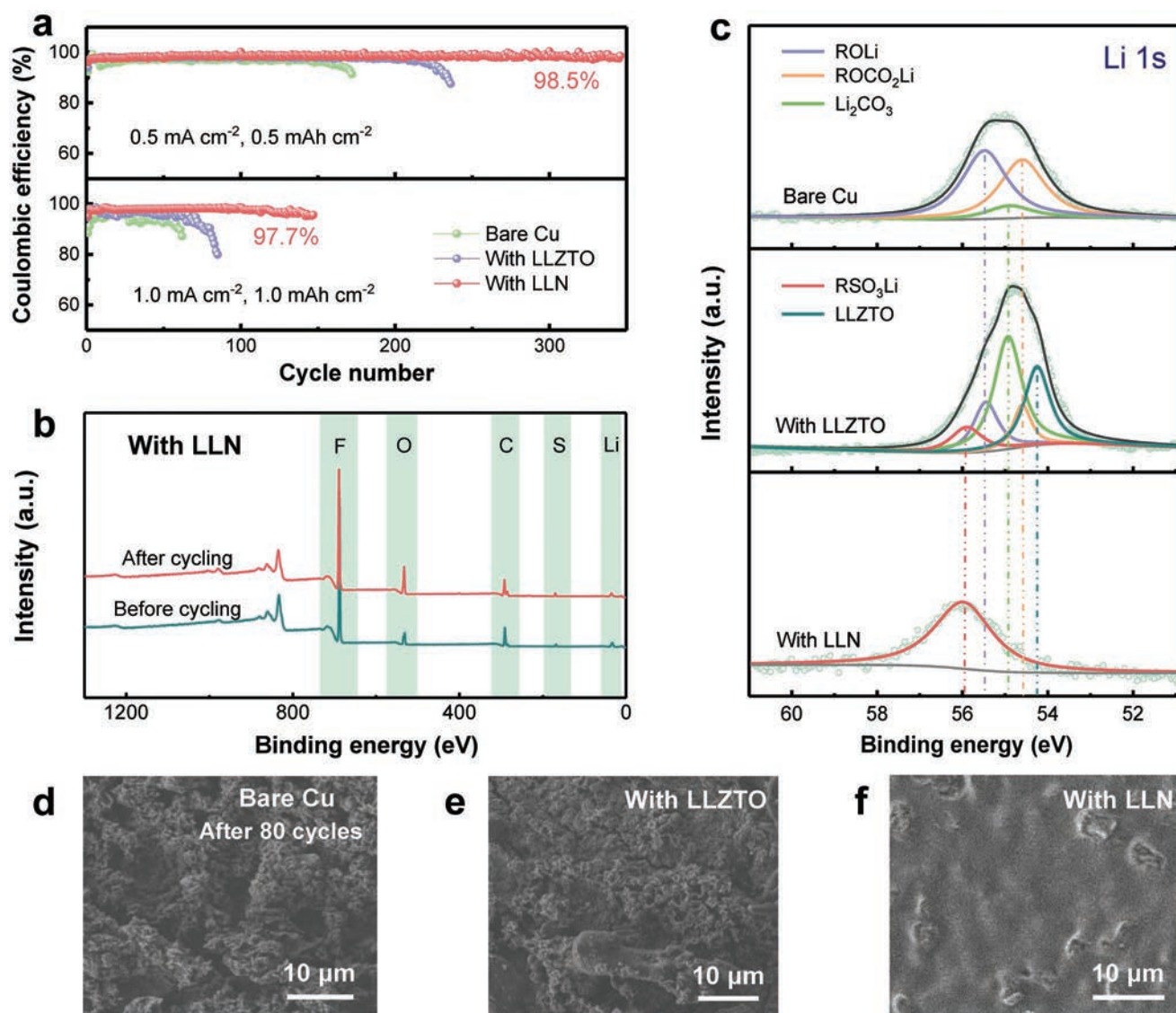


Figure 3. Electrochemical performances of Li | Cu cells. a) Coulombic efficiency of bare Cu, LLZTO-coated Cu, and LLN-coated Cu at various current densities. b) XPS characterizations of LLN-coated Cu before and after 20 cycles at 1.0 mA cm⁻², 1.0 mAh cm⁻², and c) Li 1s spectrum of the cycled Cu foil with various modifications. d–f) SEM images of bare Cu (d), LLZTO-coated Cu (e), and LLN-coated Cu (f) after 80 cycles at 1.0 mA cm⁻², 1.0 mAh cm⁻².

distribution are already widely verified to be critical on flat Li plating.^[24]

Li | Cu cells are commonly adopted to investigate the cycling efficiency of Li metal anode. The higher coulombic efficiency (CE) and longer lifespan of Li | Cu cells are indicators of a more stable Li plating behavior with more plated Li available for the subsequent stripping. A systematic study was conducted to disclose the effects of interfacial properties on the stability of Li metal by carefully comparing the electrochemical performance of bare Cu, LLZTO-coated Cu, and LLN-coated Cu. Note that the individual LLZTO coating layer can also render a high t_{Li^+} of 0.85 similar to that of LLN coating (Figure S6c, Supporting Information), which is attributed to the unique vacancy Li⁺-conducting mechanism in the bulk garnet electrolyte. As shown in Figure 3a, the unprotected cell exhibited the worst stability with CE dropping to 91.4% within only 170 cycles at a constant

current density of 0.50 mA cm⁻² and a total Li plating amount of 0.50 mAh cm⁻². After the protection of LLZTO, an enhanced performance with an average CE of 97.9% for 220 cycles can be achieved, which is believed to be originated from the optimized Li plating process guaranteed by the combined superiority of LLZTO, i.e., the single-ion-conducting nature as well as high mechanical rigidity.

To confirm this synergistic effect brought by the LLZTO coating, cells modified with sole Li-Nafion soft layer were assembled for comparison, the t_{Li^+} of which was determined to be 0.82 (Figure S8 and Table S1, Supporting Information). There are fluctuant CEs within only 200 cycles (Figure S9, Supporting Information), indicating the significance of the rigidity of LLZTO on the stabilization of Li metal upon long-term cycling. Exclusively, such a stable performance can be dramatically prolonged to more than 350 cycles once modifying

the Cu current collector with the dual-layer LLN coating, where the average CE is determined to be as high as 98.5%. The voltage–time curves are provided in Figure S10 (Supporting Information), which indicate a stable voltage hysteresis of the LLN-protected cell even at the 300th cycle (Figure S9b, Supporting Information).

Furthermore, a Li | Cu cell protected by the LLN coating delivered a stable cycling for over 150 cycles with an average CE of 97.7% when the current density and areal capacity were increased to 1.0 mA cm⁻² and 1.0 mAh cm⁻², respectively. In contrast, the CE of the unprotected cell and LLZTO-protected cell quickly decayed to below 90% within 60 and 80 cycles, respectively. Even at a higher current density of 2.0 mA cm⁻², the LLN-protected cell still displayed a decent CE of 95.2% after 80 cycles, far beyond that of the control sample (Figure S11, Supporting Information). Additionally, various dual-phase configurations were also examined in Li | Cu cells, where the configuration composed of LLZTO-based bottom layer and Li-Nafion top layer exhibited the best cell performance over that of the dual-layered film composed of Li-Nafion bottom layer and LLZTO-based top layer as well as the mono-layered LLZTO/Li-Nafion composite film (Figure S12, Supporting Information).

Note that both of LLZTO and LLN coatings are equipped with high Li⁺ transference number and superior mechanical strength. To uncover the underlying reasons for such a remarkable performance distinction, post-mortem X-ray photoelectron spectroscopy (XPS) analysis and SEM observations were carried out on the cycled Cu foils with various modifications. As expected, the interfacial composition of LLN-coated Cu maintained consistent before and after cycling (Figure 3b), indicating the superb structural integrity of LLN film during long-term charging/discharging processes. In contrast, the LLZTO-coated Cu displayed a distinctive spectrum after cycling (Figure S13, Supporting Information). In Li 1s spectrum of the LLN-coated Cu, peak only arose at 55.9 eV, which was rationally assigned to the Li⁺ containing in Li-Nafion (Figure 3c, bottom), echoing with its S 2s spectrum to confirm that Li-Nafion is the only Li-containing component present on the surface of the cycled LLN-coated Cu (Figure S14, Supporting Information). However, multiple components of RO-Li (55.5 eV), ROCO₂-Li (54.6 eV), and Li₂CO₃ (54.9 eV) were detected on the LLZTO-coated Cu besides the original components of LLZTO as well as a limited amount of Li-Nafion binder (Figure 3c, middle). The same components can also be observed on the cycled bare Cu (Figure 3c, top). The corresponding C 1s spectrum of the LLZTO-coated Cu after cycling (Figure S15, Supporting Information) further confirmed the existence of these SEI components.

The morphologies of the modified/unmodified Cu foil after long-term Li plating/stripping were also recorded (Figure 3d–f). Identical loose and porous structure can be observed on the bare Cu (Figure 3d) and LLZTO-coated Cu (Figure 3e), which is regarded as the resistive “dead Li” entangled with thick SEI. Many cracks of the originally compact LLZTO coating can be found after repeated Li plating/stripping processes, exposing fresh Li metal to the nonaqueous electrolytes. The electrolyte consumption and heterogeneous SEI formation occurred at these cracking spots inevitably result in self-amplified dendrite growth, which got disconnected easily from the current collectors during stripping, forming porous “dead Li” just as what

occurred on the bare Cu current collectors. However, the LLN-protected Cu displayed a flat and uniform morphology even after 80 cycles under 1.0 mA cm⁻² (Figure 3f). Such an efficient protection with a superior long-term stability enabled by LLN is derived from its predominant functional advantages of single-ion-conducting nature to render a homogeneous ion flux, and structural merits combining rigid inorganic bottom layer and elastic organic top layer to further physically strengthen the interface while tolerating the volume variation.

Considering that there is heterogeneous nucleation on Cu substrate when Li is plating, which cannot exactly reflect the behavior of Li growth on lithium electrodes, symmetric Li cells are therefore employed to disclose the stability of Li plating/stripping directly on Li substrates. Ultrathin Li electrodes with a thickness of 50 μm were utilized in the following experiments to provide a harsher evaluation in the case of reduced excess Li. The LLN-protected Li exhibited a slightly higher initial polarization of 90 mV (65 mV for bare Li) under the constant current density of 1.0 mA cm⁻², which slowly decreased to as low as 45 mV at 100 h, even lower than the initial value of the control sample (Figure 4a). This is believed to be as a result of the restrained concentration gradient formation and high-efficiency transport of Li⁺ at the interface during long-term cell operation. In contrast, the bare symmetric Li cell displayed a gradual increased polarization to 84 mV at 100 h, finally breaking down within 120 h. Longer galvanostatic time for 3 h was further examined in symmetric Li cell at 1.0 mA cm⁻², and a stable polarization of the LLN-protected cell was also obtained as illustrated in Figure S16 (Supporting Information). Even at higher current densities of 2.0 and 3.0 mA cm⁻², considerable performance with small polarization (95 and 128 mV, respectively) of the protected cells can be still gained (Figure S17, Supporting Information).

Electrochemical impedance spectroscopy (EIS) was carried out to provide more insights on the cell performance. The real axis intercept of the as-obtained EIS plot represents the bulk resistance of the liquid electrolyte, while the semi-circle is related to the interfacial resistance. As depicted in Figure S18 (Supporting Information), the initial interfacial resistance of both cells decreased due to the higher surface area of the electrode after cycling. Nevertheless, what differs is that the unprotected cell displayed a remarkable growth in bulk resistance after cycling for 100 h (Figure 4b), which is associated with the excessive consumption of liquid electrolyte and the accumulation of thick “dead Li,” significantly impeding the bulk transfer of Li⁺. However, this phenomenon can be greatly alleviated by incorporating LLN coating layer, where a nearly constant bulk resistance can be observed upon cycling. The conclusions drew in the EIS analysis can be further supported by the distinctive morphology observed on the unprotected (Figure 4c) and LLN-protected Li (Figure 4d) after 100 h cycling. Thick “dead Li” formation is noticed from the side view of the cycled bare Li, in accordance with the polarization augment and fluctuation, whereas the LLN-protected one still remained a relatively compact morphology.

Full cells were assembled for an assessment of the LLN-protection strategy under practical conditions. Ultrathin (50 μm) Li anode, LiFePO₄ (LFP) cathode, and conventional carbonate electrolyte of 1.0 M LiPF₆-EC/DEC (v:v = 1/1) were

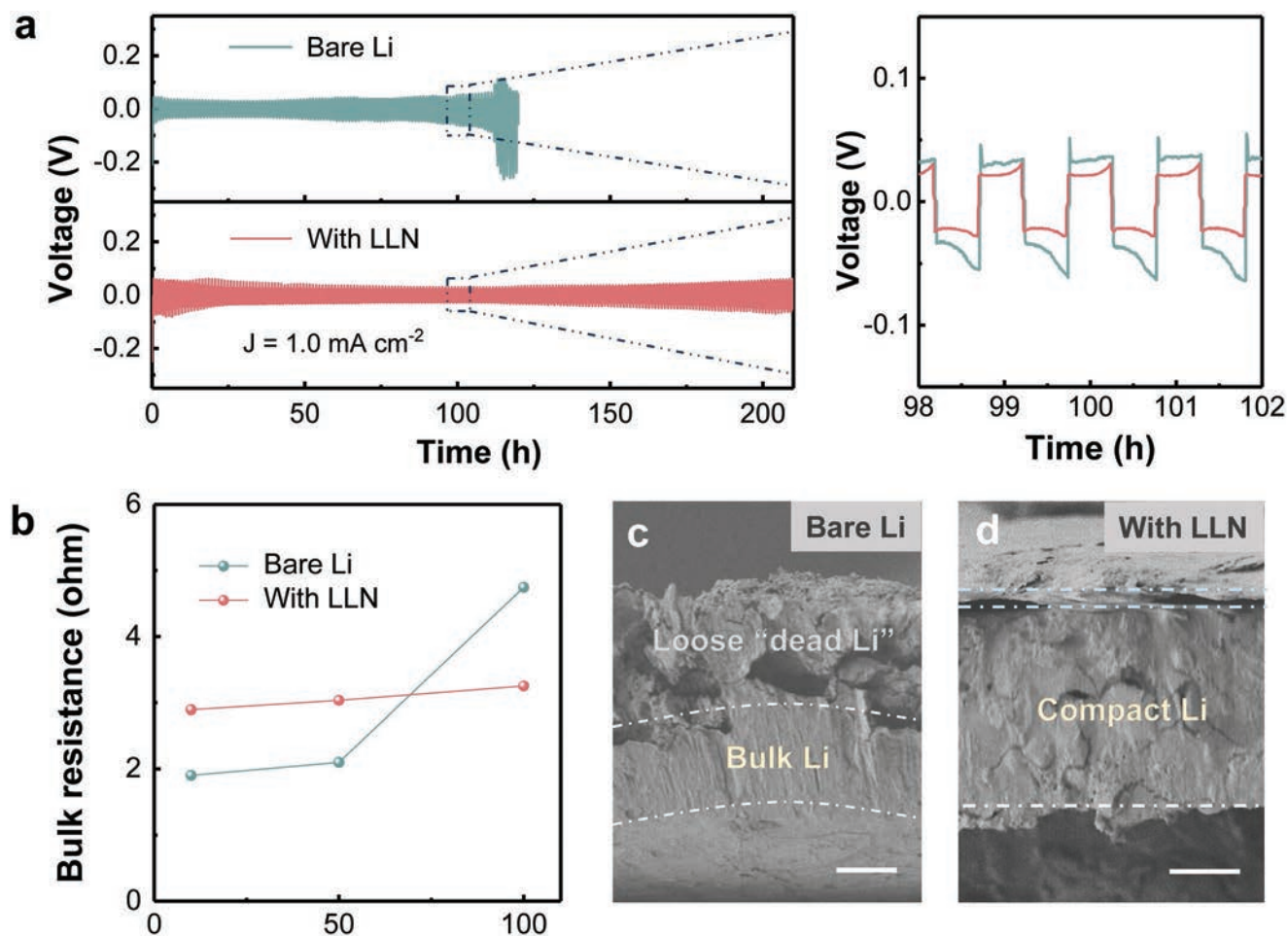


Figure 4. Electrochemical performances of symmetric Li cells with 50 μm thick Li foils. a) Cell performance of bare Li and LLN-coated Li at 1.0 mA cm^{-2} , 0.5 mAh cm^{-2} and the local enlarged voltage–time curve at 100 h. b) The bulk resistance variation after the 10th, 50th, and 100th cycles obtained from equivalent circuit fitting. Side-view SEM images of c) bare Li and d) LLN-coated Li after 100 h cycling, the scale bars of which are 20 μm .

adopted in the cell assembly. As can be seen from **Figure 5a**, the capacity of bare Li began to sharply decline from only 60th cycle at 1 C, which reflects the extremely instability of Li in highly corrosive carbonate electrolyte. However, once disassembling the cycled cell and pairing the cycled cathode with a fresh Li metal, the capacity can recover to 120 mAh g^{-1} , inferring that anode exhaust together with electrolyte consumption is the major factor responsible for the evident capacity fading. The depletion of active Li and liquid electrolyte strongly suggests the unstable electrode/electrolyte interface, which directly induces proliferate parasitic reactions and dendrite growth. In contrast, the LLN-protected Li delivered a significantly more stable cycling with a suppressed capacity decline from 135 to 120 mAh g^{-1} at the 150th cycle, equaling to a capacity retention of 87.4%. This discrepancy on cell degradation can be further explained in the voltage profiles at the and the 100th cycle (**Figure 5b**), where the voltage polarization of LLN-protected cell increased much more slowly than that of the unprotected cell. This is on account of the well-suppressed electrolyte consumption and “dead Li” accumulation upon cell operation, as has been confirmed in the previous symmetric Li cell tests.

Rate performance was also studied to probe the influence of as-proposed LLN coating on cell capacity (**Figure 5c**). Initially, the cells with and without LLN protection exhibited nearly the same capacities of 157 (0.1 C) and 156 mAh g^{-1} (0.2 C). However, higher capacities of 148 , 135 , and 116 mAh g^{-1} were obtained in the case of LLN-protected cell at 0.5 , 1 , and 2 C , respectively. When resetting to 0.1 C , the cell protected by LLN recovered to a considerable capacity of 158 mAh g^{-1} , a bit higher than the control sample of 155 mAh g^{-1} . The voltage polarizations of the protected/unprotected cells were further investigated (**Figure 5d**). A slightly larger polarization of 82 mV was observed of the LLN-protected cell comparing to 72 mV of the cell with bare Li at 0.1 C . However, it became comparable to that of the control cell at 0.2 C . Thereafter, the LLN-protected cell displayed a lower polarization (195 mV) than the unprotected one (217 mV) at 0.5 C , and the gap gradually increased with the increasing of the current density. The polarization voltages of 322 mV (protected) versus 386 mV (unprotected) at 1 C and 620 mV (protected) versus 705 mV (unprotected) at 2 C were recorded. The suppressed polarization augment observed upon current increase can be explained from two aspects: (1) The LLN coating is expected to prevent aggressive electrolyte

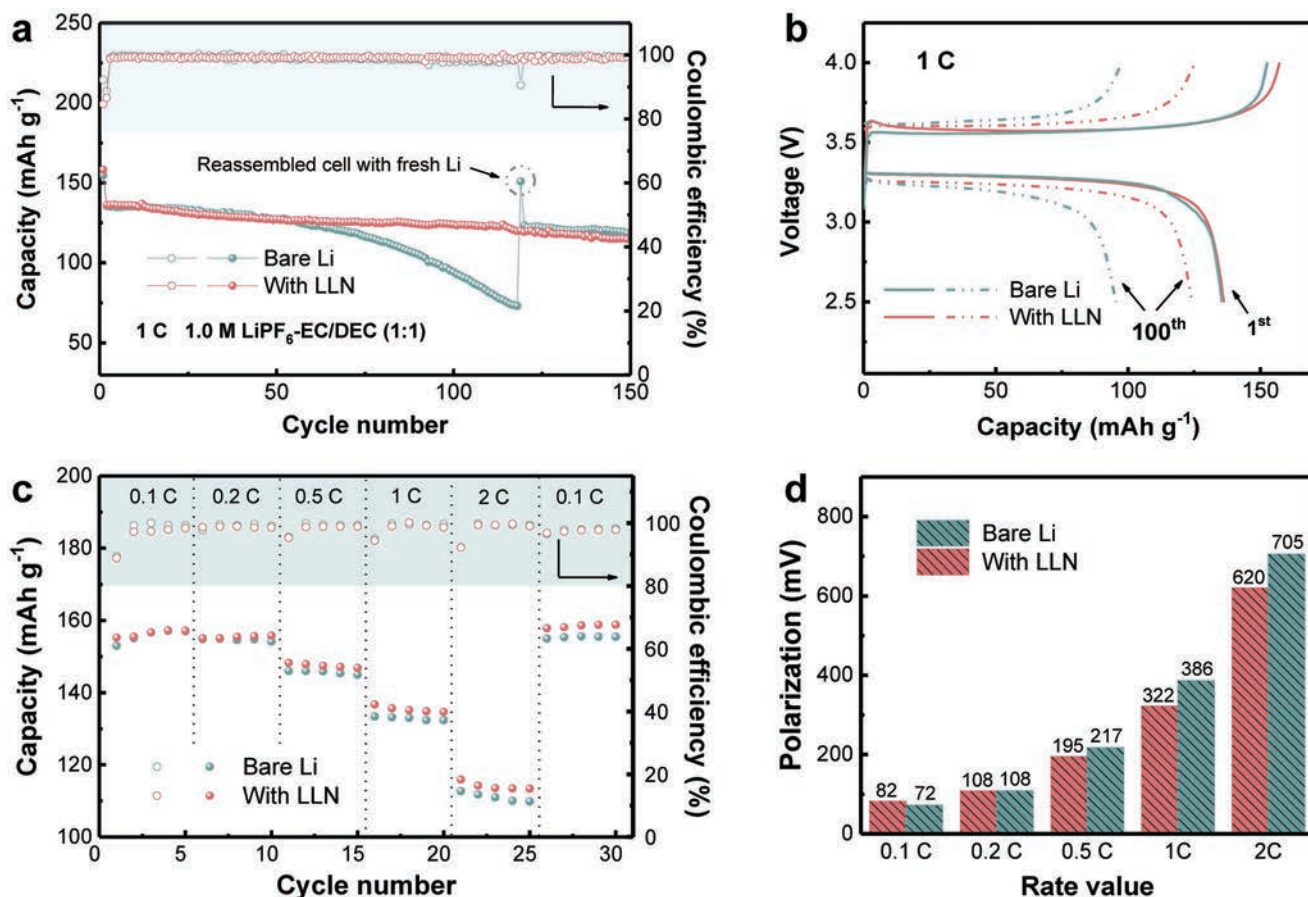


Figure 5. Electrochemical performances of Li | LFP full cells with limited Li excess. a) Specific capacity of Li | LFP cells with bare Li and LLN-coated Li at 1 C rate using conventional carbonate electrolyte; b) the corresponding voltage–capacity curves at the 1st and 100th cycles. c) Rate performance of Li | LFP cells with bare Li and LLN-coated Li at 0.1, 0.2, 0.5, 1, and 2 C; d) a comparison of the corresponding voltage polarizations under various rates.

consumption, therefore minimizing the continuous accumulation of resistive SEI. (2) The suppression of the large Li-ion concentration gradient formation enabled by the single-ion-conductive artificial film is believed to facilitate a facile Li-ion transport at the anode surface even under high current densities.

It is claimed that the strategy of LLN protective film demonstrated herein serves as a proof of concept. It can be further rationally refined as a universal strategy of a dual-layer organic/inorganic hybrid layer, where the organic and inorganic components should meet the standards of: (1) serving as single-ion conductors, (2) endowed with sufficient thermodynamic stability against Li metal, to provide a synergistic protection for working Li metal batteries. Additionally, this strategy of constructing a dual-layer organic/inorganic protective layer can also be potentially extended as a novel capsulation strategy to effectively protect Li metal from the corrosion of air and water, which is urgent and critical for the large-scale deployment of Li metal.

In summary, a robust inorganic-rich artificial interphase with single-ion pathways was proposed to guarantee an efficient protection for Li metal anode during long-term cell operation. Multiple merits have been enabled by this advanced artificial film: (1) Primarily, the single-ion-conducting nature affords a high-efficiency transport and spatially homogeneous distribution

of Li-ion at electrode/electrolyte interface as revealed by FEM simulation, which strongly contributes to the subsequent dendrite-free Li plating mode. (2) The dense LLZTO bottom layer with high rigidity is expected to further physically reinforce the Li metal surface via mechanically smoothing the Li deposits. (3) Last but not least, the Li-Nafion top layer enables the interphase with sufficient deformability and robustness to accommodate the volume changes of the electrodes. Therefore, Li | Cu cells protected by LLN delivered a significantly improved average CE of 98.5% for more than 350 cycles, which was greatly higher than that of the unprotected cell (dropping to 91.4% within only 170 cycles). Suppressed augments in bulk resistance and “dead Li” layer thickness during long-term cycling were also observed in the LLN-protected symmetric Li cells. The LLN-protected cell demonstrated a stable cycling with a higher capacity retention of 87.4% after 150 cycles in the practical full cell with ultrathin Li anode and LFP cathode, while the control sample exhibited a sharp capacity decrease from only 60th cycle.

This work elucidates the significance of optimizing the interfacial property on the stabilization of Li metal anode, which is expected to provide a deeper insight on the protection of Li metal. Moreover, this strategy of constructing a rationally designed dual-layer artificial protective layer is also implantable to the interfacial protection of other alkali metal (sodium)-based

battery systems through facilely replacing the Li single-ion conductors with sodium single-ion conductors.

Supporting Information

Supporting Information is available from the Wiley Online Library or from the author.

Acknowledgements

R.X. and Y.X. contributed equally to this work. This work was supported by the National Key Research and Development Program (2016YFA0202500), the National Natural Science Foundation of China (21776019, 21825501, and 21805161), Beijing Natural Science Foundation (L182021), and the Beijing Key Research and Development Plan (Z181100004518001).

Conflict of Interest

The authors declare no conflict of interest.

Keywords

lithium-metal anodes, rechargeable batteries, single-ion pathways, solid electrolyte interphase

Received: December 31, 2018

Revised: February 20, 2019

Published online:

- [1] B. Dunn, H. Kamath, J. M. Tarascon, *Science* **2011**, 334, 928.
- [2] M. S. Whittingham, *Chem. Rev.* **2004**, 104, 4271.
- [3] a) Y. Zhu, S. Wang, Z. Miao, Y. Liu, S. L. Chou, *Small* **2018**, 14, 1801987; b) L. Ma, T. Yu, E. Tzoganakis, K. Amine, T. Wu, Z. Chen, J. Lu, *Adv. Energy Mater.* **2018**, 8, 1800348; c) Z. W. Zhang, H. J. Peng, M. Zhao, J. Q. Huang, *Adv. Funct. Mater.* **2018**, 28, 1707536; d) X. Shen, H. Liu, X. B. Cheng, C. Yan, J. Q. Huang, *Energy Storage Mater.* **2018**, 12, 161.
- [4] a) L. Li, S. Li, Y. Lu, *Chem. Commun.* **2018**, 54, 6648; b) W. Xu, J. Wang, F. Ding, X. Chen, E. Nasybutin, Y. Zhang, J. G. Zhang, *Energy Environ. Sci.* **2014**, 7, 513.
- [5] a) M. D. Tikekar, S. Choudhury, Z. Tu, L. A. Archer, *Nat. Energy* **2016**, 1, 16114; b) X. Yu, A. Manthiram, *Energy Environ. Sci.* **2018**, 11, 527; c) X. B. Cheng, C. Yan, X. Q. Zhang, H. Liu, Q. Zhang, *ACS Energy Lett.* **2018**, 3, 1564; d) K. Xu, *Chem. Rev.* **2014**, 114, 11503; e) X. Fan, L. Chen, O. Borodin, X. Ji, J. Chen, S. Hou, T. Deng, J. Zheng, C. Yang, S.-C. Liou, K. Amine, K. Xu, C. Wang, *Nat. Nanotechnol.* **2018**, 13, 715.
- [6] a) J. B. Goodenough, Y. Kim, *Chem. Mater.* **2010**, 22, 587; b) D. Aurbach, A. Zaban, Y. Gofer, Y. Ein-Ely, I. Weissman, O. Chusid, O. Abramson, *J. Power Sources* **1995**, 54, 76.
- [7] a) S. Wei, S. Choudhury, Z. Tu, K. Zhang, L. A. Archer, *Acc. Chem. Res.* **2018**, 51, 80; b) D. Aurbach, Y. Gofer, J. Langzam, *J. Electrochem. Soc.* **1989**, 136, 3198; c) Y. Li, Y. Li, A. Pei, K. Yan, Y. Sun, C. L. Wu, L. M. Joubert, R. Chin, A. L. Koh, Y. Yu, J. Perrino, B. Butz, S. Chu, Y. Cui, *Science* **2017**, 358, 506.
- [8] a) C. Wang, Y. S. Meng, K. Xu, *J. Electrochem. Soc.* **2019**, 166, A5184; b) N. W. Li, Y. X. Yin, C. P. Yang, Y. G. Guo, *Adv. Mater.* **2016**, 28, 1853; c) Q. Pang, L. Zhou, L. F. Nazar, *Proc. Natl. Acad. Sci. USA* **2018**, 115, 5343; d) Y. Yuan, F. Wu, Y. Bai, Y. Li, G. Chen, Z. Wang, C. Wu, *Energy Storage Mater.* **2019**, 16, 411.
- [9] a) N. W. Li, Y. Shi, Y. X. Yin, X. X. Zeng, J. Y. Li, C. J. Li, L. J. Wan, R. Wen, Y. G. Guo, *Angew. Chem., Int. Ed.* **2018**, 57, 1505; b) R. Xu, X. Q. Zhang, X. B. Cheng, H. J. Peng, C. Z. Zhao, C. Yan, J. Q. Huang, *Adv. Funct. Mater.* **2018**, 28, 1705838; c) F. Wu, Y. X. Yuan, X. B. Cheng, Y. Bai, Y. Li, C. Wu, Q. Zhang, *Energy Storage Mater.* **2018**, 15, 148.
- [10] A. Kushimaa, K. P. So, C. Su, P. Bai, N. Kuriyamac, T. Maebashi, Y. Fujiwara, M. Z. Bazant, J. Li, *Nano Energy* **2017**, 32, 271.
- [11] a) Z. Sun, S. Jin, H. Jin, Z. Du, Y. Zhu, A. Cao, H. Ji, L. J. Wan, *Adv. Mater.* **2018**, 30, 1800884; b) R. Zhang, N. W. Li, X. B. Cheng, Y. X. Yin, Q. Zhang, Y. G. Guo, *Adv. Sci.* **2017**, 4, 1600445; c) L. Liu, Y. X. Yin, J. Y. Li, N. W. Li, X. X. Zeng, H. Ye, Y. G. Guo, L. J. Wan, *Joule* **2017**, 1, 563; d) R. Zhang, X. Chen, X. Shen, X. Q. Zhang, X. R. Chen, X. B. Cheng, C. Yan, C. Z. Zhao, Q. Zhang, *Joule* **2018**, 2, 764; e) C. Yang, Y. Yao, S. He, H. Xie, E. Hitz, L. Hu, *Adv. Mater.* **2017**, 29, 1702714; f) D. Lin, Y. Liu, Z. Liang, H. W. Lee, J. Sun, H. Wang, K. Yan, J. Xie, Y. Cui, *Nat. Nanotechnol.* **2016**, 11, 626.
- [12] a) X. Q. Zhang, X. B. Cheng, Q. Zhang, *Adv. Mater. Interfaces* **2018**, 5, 1701097; b) Y. Liu, D. Lin, P. Y. Yuen, K. Liu, J. Xie, R. H. Dauskardt, Y. Cui, *Adv. Mater.* **2017**, 29, 1605531.
- [13] J. N. Chazalviel, *Phys. Rev. A* **1990**, 42, 7355.
- [14] Z. Tu, S. Choudhury, M. J. Zachman, S. Wei, K. Zhang, L. F. Koukoutsis, L. A. Archer, *Joule* **2017**, 1, 394.
- [15] C. Brissot, M. Rosso, J. N. Chazalviel, S. Lascaud, *J. Power Sources* **1999**, 81–82, 925.
- [16] a) R. Bouchet, S. Maria, R. Meziane, A. Aboulaich, L. Lienafa, J. P. Bonnet, T. N. T. Phan, D. Bertin, D. Gigmes, D. Devaux, R. Denoyel, M. Armand, *Nat. Mater.* **2013**, 12, 452; b) Y. Lu, M. Tikekar, R. Mohanty, K. Hendrickson, L. Ma, L. A. Archer, *Adv. Energy Mater.* **2015**, 5, 1402073; c) C. Z. Zhao, X. Q. Zhang, X. B. Cheng, R. Zhang, R. Xu, P. Y. Chen, H. J. Peng, J. Q. Huang, Q. Zhang, *Proc. Natl. Acad. Sci. USA* **2017**, 114, 11069; d) Z. Tu, P. Nath, Y. Lu, M. D. Tikekar, L. A. Archer, *Acc. Chem. Res.* **2015**, 48, 2947.
- [17] a) K. K. F. Fu, Y. G. Gong, B. L. Liu, Y. Zhu, S. Xu, Y. Yao, W. Luo, C. Wang, S. D. Lacey, J. Dai, Y. Chen, Y. Mo, E. Wachsman, L. Hu, *Sci. Adv.* **2017**, 3, e1601659; b) J. Xiang, Y. Zhao, L. Yuan, C. Chen, Y. Shen, F. Hu, Z. Hao, J. Liu, B. Xu, Y. Huang, *Nano Energy* **2017**, 42, 262.
- [18] V. Thangadurai, S. Narayanan, D. Pinzaru, *Chem. Soc. Rev.* **2014**, 43, 4714.
- [19] Y. Li, B. Xu, H. Xu, H. Duan, X. Lu, S. Xin, W. Zhou, L. Xue, G. Fu, A. Manthiram, J. B. Goodenough, *Angew. Chem., Int. Ed.* **2017**, 56, 753.
- [20] J. Gao, C. Sun, L. Xu, J. Chen, C. Wang, D. Guo, H. Chen, *J. Power Sources* **2018**, 382, 179.
- [21] R. Murugan, V. Thangadurai, W. Weppner, *Angew. Chem., Int. Ed.* **2007**, 46, 7778.
- [22] X. Mao, L. Shi, H. Zhang, Z. Wang, J. Zhu, Z. Qiu, Y. Zhao, M. Zhang, S. Yuan, *J. Power Sources* **2017**, 342, 816.
- [23] a) M. D. Tikekar, L. A. Archer, D. L. Koch, *Sci. Adv.* **2016**, 2, e1600320; b) Q. Pang, X. Liang, A. Shyamsunder, L. F. Nazar, *Joule* **2017**, 1, 871.
- [24] a) W. Liu, D. Lin, A. Pei, Y. Cui, *J. Am. Chem. Soc.* **2016**, 138, 15443; b) X. B. Cheng, T. Z. Hou, R. Zhang, H. J. Peng, C. Z. Zhao, J. Q. Huang, Q. Zhang, *Adv. Mater.* **2016**, 28, 2888; c) W. Zhang, H. L. Zhuang, L. Fan, L. Gao, Y. Lu, *Sci. Adv.* **2018**, 4, eaar4410.